

1
2
3
4
5
6
7
8
9
10
11
12
13
14
15
16
17
18
19
20
21
22
23
24
25
26
27
28
29
30
31
32
33
34

**Origin and significance of Si and O isotope heterogeneities
in Phanerozoic, Archean, and Hadean zircon**

Dustin Trail^{1,2,*}, Patrick Boehnke^{3,4}, Paul S. Savage⁵,
Ming-Chang Liu², Martha L. Miller¹, Ilya Bindeman⁶

¹Department of Earth & Environmental Sciences
University of Rochester, Rochester, NY 14627, USA

²Department of Earth, Planetary and Space Sciences,
University of California, Los Angeles, CA, USA

³Department of the Geophysical Sciences,
The University of Chicago, Chicago, IL 60637

⁴Chicago Center for Cosmochemistry, Chicago, IL

⁵School of Earth and Environmental Sciences,
University of St Andrews, UK

⁶Department of Earth Sciences,
University of Oregon, Eugene, OR, 97403, USA

* dtrail@ur.rochester.edu; ph 585 276 7182

35 **Abstract** Hydrosphere interactions and alteration of the terrestrial crust likely played a critical
36 role in shaping Earth's surface, and in promoting prebiotic reactions leading to life, before 4.03
37 Ga (the Hadean Eon). The identity of aqueously-altered material strongly depends on
38 lithospheric cycling of abundant and water-soluble elements such as Si and O. However, direct
39 constraints that define the character of Hadean sedimentary material are absent because samples
40 from this earliest eon are limited to detrital zircons ($ZrSiO_4$). Here we show that concurrent
41 measurements of Si and O isotope ratios in Phanerozoic and detrital pre-3.0 Ga zircon constrain
42 the composition of aqueously-altered precursors incorporated into their source melts.
43 Phanerozoic zircon from (S)edimentary-type rocks contain heterogenous $\delta^{18}O$ and $\delta^{30}Si$ values
44 consistent with assimilation of metapelitic material, distinct from the isotopic character of zircon
45 from (I)gneous- and (A)norogenic-type rocks. The $\delta^{18}O$ values of detrital Archean zircons are
46 heterogenous, though yield Si isotope compositions like mantle-derived zircon. Hadean crystals
47 yield elevated $\delta^{18}O$ values (vs. mantle zircon) and $\delta^{30}Si$ values span almost the entire range
48 observed for Phanerozoic samples. Coupled Si and O isotope data represent a new constraint on
49 Hadean weathering and sedimentary input into felsic melts including re-melting of amphibolites
50 possibly of basaltic origin, and fractional addition of chemical sediments, such as cherts and/or
51 Banded Iron Formations (BIFs) into source melts. That such sedimentary deposits were
52 extensive enough to change the chemical signature of intracrustal melts suggests they may have
53 been a suitable niche for (pre)biotic chemistry as early as 4.1 Ga. **(248 words)**

54

55 Key words; Hadean; zircon; weathering; Silica cycle; origin of life; Lachlan Fold Belt

56

57

58

59 **Significance**

60 The crust or its chemically weathered derivatives likely served as a substrate for the origin of
61 life, which could have occurred by 4.1 Ga. Yet no known *bona fide* terrestrial rocks from this
62 time remain. Studies have thus turned to geochemical signatures within detrital zircons from this
63 time. While zircons do not directly record low-temperature weathering processes, they inherit
64 isotopic information upon recycling and re-melting of sediment. We developed a method to
65 fingerprint the identity of material involved in water-rock interactions >4 Ga, bolstered by a
66 large Si and O isotopic dataset of more modern zircon samples. The data presented here provide
67 evidence for chemical sediments, such as cherts and Banded Iron Formations on Earth >4 Ga.

68 **(117 words)**

69

70 \body

71 **Introduction**

72 In the apparent absence of a pre-4.0 Ga terrestrial rock record, early speculations about
73 the Hadean Earth (~4.5-4.0 Ga) were drawn from meteorites and backward extrapolation of
74 preserved Archean rocks. Insights into the nature of the Hadean surface environment relied on
75 broad estimates of mantle heat production and its transport to the surface, and scaling of the
76 lunar impact record to the early Earth (1). Laboratory simulations predicted intense meteorite
77 bombardment and a thick steam-rich atmosphere (2), suggesting that Earth may not have been
78 continuously habitable in the first 500 Myr (3).

79 The first direct constraints on the geology of the young Earth came from the discovery of
80 Hadean detrital zircons (4). Subsequent *in situ* oxygen isotope measurements of some Hadean

81 zircon yielded isotopically heavy compositions, relative to the canonical mantle value (5,6). Such
82 isotopic shifts provide evidence for water-rock interactions at low temperatures (*sensu lato*),
83 followed by re-melting and incorporation of these signatures into Hadean zircon parent melts by
84 4.2 to 4.3 Ga (5-8). More recent numerical calculations that evaluate early Earth heat transfer
85 and plausible chemical reactions (9), the thermal effects of terrestrial impact metamorphism (10),
86 and a re-evaluation of lunar impact chronology (11) continue to strengthen the case a
87 continuously habitable planet shortly after accretion.

88 Such discoveries are important, although many uncertainties remain regarding Earth's
89 earliest development. This highlights the need to find new ways to better constrain Earth's
90 primordial geology. For instance, only limited information about the identity of weathered
91 material involved in the zircon source melt is provided by mildly elevated Hadean $\delta^{18}\text{O}$ values,
92 which are up to ~ 2 ‰ above present-day mantle zircon. This is because almost all surficial/low-
93 temperature water-rock interactions result in an isotopically heavy O composition being imparted
94 on the rock. Constraining the identity of weathered Hadean material is timely due to the
95 suggestion that an isotopically light carbon inclusion in a ~ 4.1 Ga zircon may indicate the
96 presence of a biosphere (12), implying the need for a suitable substrate for life by this time.

97 Silicon isotopes, like O isotopes, are also strongly fractionated during chemical
98 weathering of silicate material or low temperature water-rock interactions (SI Appendix, Fig.
99 S1). Given the dominance of O and Si in the lithosphere, the composition of altered or
100 weathered products strongly depends on reactions that involve both elements. First, consider
101 that neoformation of clay minerals prefers the lighter Si isotopes, and the degree of fractionation
102 is magnified with the extent of weathering degree/amount of desilicification to more negative
103 $\delta^{30}\text{Si}$ values (i.e. 1:1 clays such as kaolinite are much lighter than 2:1 clay minerals, 13-15). This

104 gives Si isotopes the added advantage over O isotopes alone as they have the potential to be a
105 definitive proxy for identifying the presence of pelitic sediment in a melt source (Fig. 1, path 1).
106 Second, unlike O isotopes, Si isotopes are unaffected during hydration of primary silicates (i.e.
107 serpentinization) and at low weathering degrees, where igneous minerals still dominate the Si
108 isotope signature (16; Fig. 1, path 2). Third, precipitation and diagenesis of authigenic silica and
109 hydrothermal silicification can lead to large variations in $\delta^{30}\text{Si}$ (17-19). Under non-equilibrium
110 conditions, this can generate negative shifts in $\delta^{30}\text{Si}$, but unlike desilicification, often there may
111 be no correlation between Si and O variations in the silica, due to the different behavior of these
112 elements under different rock/water ratios and temperatures (18). Finally, Si isotopes have
113 another advantage over O isotopes alone because seawater-derived authigenic silica (i.e., chert)
114 reveals uniquely heavy Si isotope compositions (e.g. 20; Fig. 1, path 3). These Si-O isotope
115 fractionation pathways – shown schematically in Figure 1 – demonstrate the critical advantage of
116 coupled Si-O isotope analysis.

117 Melt assimilation of the weathered products described above may be used to explore past
118 environments only if the isotopic composition of the whole rock (WR) and minerals – including
119 zircon – partially, at least, reflect these original altered products. Such variations in WR Si
120 isotope compositions, linked unequivocally to source variation, have been measured in several
121 localities, including the Lachlan Fold Belt (21,22). Moreover, there is limited Si isotope
122 fractionation caused by partial melting and igneous fractional crystallization; mantle rocks and
123 mantle-derived melts yield identical $\delta^{30}\text{Si}$ values (Bulk Silicate Earth $\delta^{30}\text{Si} = -0.29 \pm 0.07\text{‰}$
124 relative to NBS28; 15). Felsic rocks, absent of any non-igneous assimilant, tend to be only 0.10
125 to 0.20 ‰ heavier than BSE, demonstrating there is a small and crucially predictable enrichment
126 of heavier Si isotopes due to magmatic differentiation (23). A source rock signature will be

127 recorded in zircons, provided that the difference between $\delta^{30}\text{Si}(\text{WR})$ and $\delta^{30}\text{Si}(\text{zircon})$ – i.e.,
128 $\Delta^{30}\text{Si}(\text{WR-zircon})$ – is constrained.

129 To extend the terrestrial Si isotope record back to the Hadean, we take the approach that
130 $\delta^{30}\text{Si}$ values should be considered with $\delta^{18}\text{O}$, because such coupled isotopic analyses are
131 potentially powerful in identifying the lithologies assimilated in Hadean melt sources (Fig. 1). In
132 this contribution, we report solution-based multi-collector inductively coupled plasma mass
133 spectrometry (MC-ICP-MS) measurements of mantle-derived zircon and separate felsic whole
134 rock fractions from the crust to define: (i) the Si isotopic composition of zircon that crystallized
135 in the absence of sediment inputs; and (ii) $\Delta^{30}\text{Si}(\text{WR-zircon})$, which constrains high temperature
136 Si isotope fractionations. To analyze single zircons at $\sim 20\ \mu\text{m}$ spatial resolution, we developed
137 an ion microprobe analytical protocol for simultaneous *in situ* measurements of both isotope
138 systems. First, this method was used to investigate coupled Si and O isotope compositions of *in-*
139 *context* igneous zircons from 10 different Australian Lachlan Fold Belt (LFB) Phanerozoic
140 granitoids classified as (S)edimentary, (I)gneous, and (A)norogenic (SI Appendix, Fig. S2).
141 These data, together with the Si and O isotope record of Eoarchean sediments (17,20), form the
142 basis for our interpretation of ion microprobe data for Hadean and Archean zircon. An overview
143 of measured samples is presented in SI Appendix, Table S1.

144

145 **Results**

146 Mantle-derived Mud Tank carbonatite (Australia), Kimberley pool (South Africa), and
147 Orapa Kimberlite (Botswana) zircons yield $\delta^{30}\text{Si}_{\text{NBS28}}$ values that range from -0.34 to -0.41 ‰
148 (SI Appendix, Table S2). The average $\delta^{30}\text{Si}$ value of $-0.38 \pm 0.02\ \text{‰}$ (1 s.d.), determined by MC-
149 ICP-MS, is used to define $\delta^{30}\text{Si}$ of mantle-derived zircon. The LFB Jindabyne tonalite fractions

150 yield respective $\delta^{30}\text{Si}$ values for zircon, WR, and quartz of -0.57 ± 0.02 , -0.20 ± 0.03 , and -
151 0.11 ± 0.02 ‰. This defines $\Delta^{30}\text{Si}(\text{WR-zircon}) = 0.37$ ‰ for this sample (Fig. 2), in good
152 agreement with *ab initio* Si isotope fractionation calculations (24).

153 Ion microprobe zircon Si isotope data reveal differences, albeit with overlap, between our
154 Australian LFB granitoid types (Fig. 3; SI Appendix, Table S3). Typically, S-type samples
155 contain $\delta^{30}\text{Si}$ values that extend to more negative values than I- or A-type granitoids. In the most
156 extreme cases, zircon $\delta^{30}\text{Si}$ extends down to about -1.5 ‰, as observed for the Cootralantra
157 samples. Zircons analyzed from the Bullenbalong S-type granitoid are not characterized by $\delta^{30}\text{Si}$
158 values lighter than -1.0 ‰, and in fact the overall distribution of $\delta^{30}\text{Si}$ makes it broadly
159 comparable to the $\delta^{30}\text{Si}$ range of other I-type zircons. The Cowra Granodiorite contains zircon
160 $\delta^{30}\text{Si}$ that would be most consistent with results obtained from I-type samples, except that a
161 larger fraction of the analyses is shifted toward more negative values than other I-types examined
162 thus far. I-type granitoids have a similar dispersion in $\delta^{30}\text{Si}$ as S-types, though zircon $\delta^{30}\text{Si}$
163 distributions are shifted towards heavier values, and several data are within error of 0 ‰. Except
164 for Cowra zircons, no S-type analyses are within error of 0 ‰. The A-type sample (Watergums)
165 and Duluth Gabbro yield tighter $\delta^{30}\text{Si}$ distributions when compared to I- and S-type ranges for a
166 similar number of data points. S- and I-type O isotope data, collected ‘simultaneously’ with Si
167 isotopes, also show distinct differences (Fig. 4; SI Appendix, Fig. S4). S-type zircons typically
168 yield $\delta^{18}\text{O}_{\text{VSMOW}}$ values from $+8$ to 10.5 ‰, whereas I- and A-types are typically confined to
169 $\delta^{18}\text{O}$ values of $+6$ to 8.5 ‰.

170 Individual ion microprobe spot data ($n = 79$) for Jack Hills zircons consist of 14 zircons
171 ≥ 4.0 Ga, and 21 Archean grains (SI Appendix, Table S4), and reveal subtle isotopic differences
172 among the two age groups (Fig. 5; SI Appendix, Fig. S4). Specifically, the Archean zircon $\delta^{18}\text{O}$

173 values are between +5.2 to +6.8‰, comparable to previous Jack Hills zircon studies (25). The
174 $\delta^{30}\text{Si}$ values of Archean zircon are broadly confined to those like mantle-derived zircon. Most
175 Hadean samples yield $\delta^{18}\text{O}$ values that range from +6 to 7 ‰ and same grains exhibit both
176 enrichments and depletions in ^{30}Si relative to mantle zircon and show a broadly similar range as
177 Phanerozoic zircon.

178

179 **Discussion**

180 **Phanerozoic ‘in-context’ zircons**

181 The well-studied Lachlan Fold Belt represents an ideal test target to demonstrate *in situ*
182 zircon-scale investigations. Coupled Si and O isotope studies of zircon have not been conducted
183 previously, so an obvious question is whether these zircon data lead to broadly similar
184 interpretations when compared to WR geochemical studies. The WR Si isotope data show that
185 S-type granitoids are, on average, isotopically lighter than I- and A-type samples, although the
186 range of Si isotopes in S-type granitoid WR extends to lower and slightly higher $\delta^{30}\text{Si}$ values
187 than the other two granitoid types (21; SI Appendix, Fig. S1).

188 Using felsic rock isotope fractionation relationships of $\Delta^{18}\text{O}(\text{WR-zircon}) \approx 2$ ‰ (27), and
189 $\Delta^{30}\text{Si}(\text{WR-zircon}) \approx 0.37$ ‰ (see Fig. 2) we find that S-type zircon, on average, predicts the most
190 negative WR $\delta^{30}\text{Si}$ and most elevated $\delta^{18}\text{O}$ WR values. This result is consistent with assimilation
191 of pelitic material (e.g., Fig. 1, path 1), and WR data for the region (20). For example, averaging
192 the results from S-type Shannons Flat zircons (Fig. 3; SI Appendix, Fig. S3) predicts respective
193 WR $\delta^{30}\text{Si}$ and $\delta^{18}\text{O}$ values of -0.45 ‰ and +10.4 ‰. A $\delta^{30}\text{Si}$ value of -0.45 ‰ is the lowest
194 estimated WR value of the 10 granitoids explored here, and is in broad agreement with the
195 lowest WR $\delta^{30}\text{Si}$ values so far reported in the LFB (SI Appendix, Fig. S1). Moreover, predicted

196 WR values from S-type zircons imply another sedimentary source besides Ordovician sediments
197 in close association with the LFB granitoids, also consistent with conclusions reached using WR
198 data only (21). Similar agreement is found for oxygen isotopes (28); other WR isotope
199 calculations for the different granitoids are reported in SI Appendix, Table S3. What is also
200 evident, especially for the I-type zircons, is the presence of an isotopically heavy Si source in
201 some regions of the Lachlan Fold Belt (e.g., Fig. 3; Glenbrog). We speculate that this is due to
202 fractional crystallization and seawater-derived authigenic silica (Fig. 1; path 3). In the latter case,
203 silica assimilation will not drive any resulting melt into the peraluminous field nor would it be
204 likely to affect Sr and Nd isotope compositions, hence the rock will still resemble an I-type, even
205 with the anatexis of ‘non-igneous’ material.

206 If individual data points are considered in lieu of averages, I- and S-type zircon Si- and
207 O- isotopes imply heterogenous isotopic values for the source rocks (Fig. 4). This is particularly
208 marked when compared to histogram ranges defined by Duluth Gabbro and A-type Watergums
209 zircon Si and O isotope data (Fig. 3; SI Appendix, Fig. S3). The petrogenesis of zircon in
210 gabbros and A-type melts is typically linked to a single (generally primitive) melt composition
211 which evolved via fractional crystallization. This homogeneous, ‘primitive’ melt composition is
212 well reflected in both suites by their mantle-like Si isotope compositions ($\delta^{30}\text{Si} \approx -0.35\text{‰}$) and
213 normal distribution (Fig. 3). In contrast, the S- and I-type LFB zircons both define wider, often
214 non-normal, data distributions. Although the lower analytical precision of *in situ* measurements
215 contributes to the apparent range, if all zircons from each I- and S-type melt had an identical Si
216 isotope composition (with perhaps minor variations due to fractional crystallization), data
217 distributions similar to that of the A-type or gabbroic zircons are expected. Hence, the wider I-
218 and S-type zircon Si and O isotope range likely reflects heterogeneities in the source, or possibly

219 multiple melt sources. This incomplete homogenization of multiple source materials in the
220 Lachlan samples is also observed in Nd, Sr, and O-isotope WR and mineral studies, which
221 underscores the hybrid nature of felsic natural systems (28,29).

222

223 **Hadean and Archean (detrital) zircons**

224 Several zircons yield $\delta^{30}\text{Si}$ values indistinguishable from mantle-derived zircon, but with
225 heavier $\delta^{18}\text{O}$ than the mantle (Fig. 5). These zircons may have crystallized from melts that
226 included assimilation of hydrated/serpentinized basalt, whereby the original 'igneous' Si isotope
227 composition of the host rocks remained unaltered, (e.g., Fig. 1, path 2). Alternatively, it was
228 suggested that low fluid/rock ratios could generate positive O isotope excursions without
229 accompanying Si isotope variation (19). Both scenarios are consistent with Hadean melts
230 (partially) influenced by source material altered by considerable hydrothermal activity.

231 Perhaps the most intriguing Hadean zircon yields a mantle-like $\delta^{18}\text{O}$ value of +5.49 ‰,
232 but records a $\delta^{30}\text{Si}$ value of -1.13 ‰ (grain 1-10). This grain represents our strongest evidence
233 for a Hadean Si reservoir out of equilibrium with the mantle. Evaluation of the $\delta^{18}\text{O}$ value only
234 would lead to the conclusion that this grain shows no evidence for interaction with an aqueous
235 reservoir, whereas $\delta^{30}\text{Si}$ suggests otherwise. We rule out fractional crystallization, as $\Delta^{30}\text{Si}(\text{WR-}$
236 $\text{zircon})$ is ~ 0.35 ‰ for felsic systems; this relationship implies a WR value of ~ -0.75 ‰. To
237 explain this result, we turn to the Archean Si isotope sedimentary record.

238 Archean cherts, which formed by chemical precipitation (and re-precipitation), have Si
239 isotope values as low as ~ -3 ‰, which also applies to Archean BIFs (17, 30-32). These
240 sediments are typically assumed to result in ^{18}O -enriched material compared to the mantle (20),
241 meaning that an ^{18}O -depleted reservoir is also required to balance the mantle-like zircon value of

242 +5.49 ‰. The Fe-oxide phases in BIFs are one possibility; these may be ¹⁸O-depleted (33),
243 which is also supported by low temperature Fe-oxide-H₂O oxygen isotope equilibrium
244 fractionations (34). Also, alteration of mafic rocks by seawater can either enrich or deplete the
245 resulting product in ¹⁸O; higher temperature (post-solidus) exchange with seawater decreases the
246 ^{δ¹⁸O} value of the altered rock (35,36). This reasoning assumes that seawater ^{δ¹⁸O} was ~0‰,
247 similar to modern (36), which is based on an assumed balance of hydrothermal and weathering
248 fluxes (37). Alternatively, at far-from-equilibrium conditions (e.g., dashed arrows in Figure 1),
249 light Si isotope compositions have been recorded in chemical precipitates where no large
250 variations in O have been recorded (38). We propose that burial and anatexis of a succession of
251 oceanic lithologies (cherts, BIFs and/or altered mafic rocks) as a possible explanation for the
252 chemistry of this 4.05 Ga zircon. A simple end-member Si isotope mixing model with basalt and
253 chemical sediment (e.g., chert) requires less than 20% of the latter to explain the range of ^{δ³⁰Si}
254 values observed in detrital zircons (SI Appendix, Fig. S5). ±

255 Zircon samples in which both ^{δ³⁰Si} and ^{δ¹⁸O} outside the ‘mantle’ zircon field are rare.
256 The most ³⁰Si enriched detrital zircon is from a 4.05 Ga grain, which is also mildly enriched in
257 ¹⁸O relative to the mantle (grain ID = 1-9, ^{δ³⁰Si} = +0.14‰; ^{δ¹⁸O} = 6.26‰). As with the positive
258 Si isotope zircons from the LFB granites, this datum implies seawater as the dominant source of
259 ^{δ³⁰Si} (Fig. 1, path 3); note that silicification of volcanogenic sediments from Archean samples
260 display more positive ^{δ³⁰Si} values that range from +0.1 to 1.1 ‰, which was also linked to
261 seawater-derived silica (20). The same study showed that Archean felsic schists are fractionated
262 to positive ^{δ³⁰Si} values, which is also qualitatively consistent with the Si- and O- isotope data for
263 this zircon.

264

265 **Conclusions**

266 In many cases, the Si isotopic measurements of crustal zircons with clear input of
267 weathered material into the source magmas, as judged by ^{18}O enrichments, exhibit $\delta^{30}\text{Si}$ values
268 indistinguishable from mantle-derived zircon. Thus, correlative analysis of Si- and O- isotopes
269 provides a more robust interpretation than either isotopic system alone; in the case of the detrital
270 grains, 'path 2' was the most common weathering trajectory. That said, a fraction of the Si
271 measured in Phanerozoic, Archean, and Hadean zircon requires assimilation of silica that
272 interacted with aqueous solutions into the melt protolith(s), ruling out Si derivation exclusively
273 from mantle sources. The range of Si and O isotope compositions recorded in the Hadean zircons
274 is consistent with melt generation from isotopically heterogeneous sources, similar to the
275 migmatite-related formation of Phanerozoic 'crustal'-derived I- and S-type granites. This is also
276 contrary to a model in which all Hadean zircon source melts were derived from isotopically
277 homogeneous mafic rocks (39).

278 The combined $\delta^{18}\text{O}$ and $\delta^{30}\text{Si}$ measurements restrict the characteristics of Hadean
279 material altered in low temperature environments. Our preferred model is that some of these
280 involved the anatexis of chemical sediments, possibly felsic schists, and (potentially silicified)
281 metabasalts. This is especially important because the early chemistry of the crust and aqueous
282 solutions are important variables that almost certainly affected early prebiotic or inorganic
283 chemical reactions (40). Archean cherts and highly metamorphosed quartz-pyroxene sediments
284 host some of the earliest proposed evidence for life associated with rocks (41,42), and an
285 isotopically light carbon inclusion within a Hadean zircon pushes record of a potential biosphere
286 back to 4.1 Ga (12). Our new evidence bolsters the case for the existence of a previously

287 undocumented suite of diverse environments – including siliceous sediments – for (pre)biotic
288 chemistry to take hold in the late Hadean.

289 **Materials and Methods**

290

291 **Zircon samples**

292 ‘Mantle’ zircons include samples from Orapa (Botswana), and Kimberley Pool, South
293 Africa (43), a megacryst from the Mud Tank carbonatite, and AS-3 zircons (45). ‘Crustal’
294 zircons were extracted from 5 S-type, 4 I-type, and 1 A-type LFB hand samples with ages from
295 395 to 436 Ma (44-48). Detailed information about sample collection location and zircon
296 geochemistry – including crystallization temperatures – is presented in the SI and elsewhere
297 (50,51). Jack Hills hand samples were collected from the classic locality (5); previously
298 published U-Pb zircon ages are presented elsewhere (51). Fragments from a large crystal from
299 Kuehl Lake (KL) were also analyzed, likely from the same locality as 91500 (52).

300 **MC-ICP-MS solution-based measurements**

301 The bulk Si isotope composition was measured using solution MC-ICP-MS techniques,
302 following previously developed methods (54,55). Sample dissolution was performed using an
303 alkali fusion method. Briefly, between 2 and 10 mg of sample powder was weighed into a silver
304 crucible (99.99% purity), accompanied by ~200 mg of semiconductor grade NaOH. The crucible
305 was placed into a muffle furnace and heated for 15 minutes at 720°C. The resultant fusion cake
306 (inside the crucible) was subsequently immersed in MQ-e water (18.2 MΩ.cm), left to
307 equilibrate overnight, then transferred into pre-cleaned polypropylene bottles. The solution was
308 diluted further in MQ-e water and acidified to 1% HNO₃ v/v.

309 Silicon was purified for isotope analysis using a single-stage cation exchange resin ion
310 chromatography procedure. Sample solutions were loaded on to BioRad Poly-Prep columns
311 containing 1.8ml of pre-cleaned BioRad AG 50W-X12 cation exchange resin (200-400 mesh).
312 As long as the sample pH is between 2-8, silicon will be in solution as a neutral or anionic
313 species and will pass straight through the resin, eluted using MQ-e water – all other major
314 element species will be in cationic form and are quantitatively retained by the resin.

315 Silicon isotopes were analyzed using a Neptune Plus (Thermo Fisher Scientific) MC-
316 ICP-MS at both the Institute de Physique du Globe de Paris (IPGP) and at the St Andrews
317 Isotope Geochemistry Laboratories (STAiG), University of St Andrews. The instruments were
318 operated in medium resolution mode (to resolve and avoid polyatomic interferences), and
319 samples were introduced into the instruments using an ESI 75 μ l.min⁻¹ PFA microflow nebulizer
320 and an SIS spray chamber. A sample concentration of 2 ppm typically resulted in a signal of
321 between ~14 and 24V on the ²⁸Si beam (using 10¹¹ Ω resistors), depending on the instrument.
322 Procedural blanks ranged from between 13 and 70 mV on the ²⁸Si beam, which is negligible
323 (<10 ppb Si) relative to the sample. Isotope ratios were measured in static mode, with each
324 measurement consisting of 25 cycles of ~3 second integrations, with a 3 second idle time.
325 Isotope measurements were calculated using the standard-sample bracketing method, with
326 NBS28 (NIST RM 8546) as the bracketing standard, in permil (‰) as follows: $\delta^x\text{Si} =$
327 $[(^x\text{Si}/^{28}\text{Si}_{\text{sample}} / ^x\text{Si}/^{28}\text{Si}_{\text{NBS28}}) - 1] \times 1000$; where x = 30 or 29, depending on the ratio.

328 Solution Si isotope data are presented in SI Appendix, Table S2. Each datum is calculated
329 as a mean of 3-5 separate measurements, and the uncertainty is calculated as the standard
330 deviation. All paired ³⁰Si and ²⁹Si data plot on a predicted mass-dependent fractionation line
331 (56), indicating that significant interferences on the isotope beams were resolved. Aliquots of

332 the standards BHVO-2 and Diatomite were consistently purified through chemistry and analyzed
333 alongside the sample unknowns. These are also given in SI Appendix, Table S2, and are identical
334 to their accepted values (15).

335 **Laser fluorination O isotope measurements**

336 Laser fluorination oxygen isotope analyses were performed at the University of Oregon
337 using a 35W CO₂-laser in a single analytical session (Oct. 2017). Zircon fragments with weights
338 of ~1.5 mg were reacted with purified BrF₅ reagent to liberate oxygen. The gases generated in
339 the laser chamber were purified through a series of cryogenic traps held at liquid nitrogen
340 temperature and a Hg diffusion pump to remove traces of fluorine gas. Oxygen was converted to
341 CO₂ gas using a small platinum-graphite converter, and then the CO₂ gas was analyzed on a
342 MAT 253 mass spectrometer. Four to seven aliquots of standards were analyzed together with
343 the unknown samples during each analytical session (for detailed analytical methods, see (57)).
344 Three UOG ($\delta^{18}\text{O} = +6.62\text{‰}$) and two Gore Mt Garnet, UWG2, ($\delta^{18}\text{O} = +5.80\text{‰}$) were used in
345 the standard set (58) and varied $\pm 0.07\text{‰}$.

346 **Ion microprobe Si and O isotope measurements**

347 Zircons were cast in epoxy along with zircon megacryst chips and AS-3. The South
348 African kimberlite (KIM) reproduced with the lowest standard deviation for Si isotopes by MC-
349 ICP-MS and was thus used as our primary matrix-matched standard for ion microprobe work.
350 Samples were gently polished by hand using disposable 1 μm Al₂O₃ polishing paper, cleaned in
351 successive ultrasonic baths of soapy water and distilled water, dried in a vacuum oven, and then
352 Au coated. A separate mount containing Jack Hills zircons was also prepared. Select crystals
353 were plucked from a pre-existing mount (51), re-cast in epoxy with standards, and polished. All

354 crystals were imaged by cathodoluminescence to help guide ion microprobe spot locations (SI
355 Appendix, Fig. S4).

356 The O and Si isotopic analyses of zircons were conducted on the UCLA CAMECA
357 *ims1290* ion microprobe. A 3 nA Cs⁺ primary beam, rastering over 10×10 μm on the samples,
358 yielded sufficient secondary ion signals (¹⁸O⁻ and ³⁰Si⁻ ≥ 6×10⁶ and 3×10⁶ counts per second,
359 respectively) to be collected with Faraday cups (FCs) in dynamic multicollection mode. This
360 configuration allows for simultaneous measurement of ¹⁶O⁻ and ¹⁸O⁻ on the L'2 and H'2 FCs,
361 respectively, followed by that of ²⁸Si⁻ and ³⁰Si⁻ on C and H1 (all FCs) after one mass jump. The
362 mass resolution (M/ΔM) was set at 2,400 (exit slit #1 on the multicollection trolley) to separate
363 molecular interferences from peaks of interest. One spot analysis is composed of 20 cycles, each
364 of which includes a counting time of 4 seconds for oxygen isotopes, and of 10 seconds for Si
365 isotopes. The backgrounds of FCs were determined during the 30 second presputtering prior to
366 each analysis, and then were corrected for in the data reduction. Secondary electron images were
367 collected after analysis (SI Appendix, Fig. S7) to verify analytical spot locations were free of
368 visible inclusions and cracks. External reproducibilities obtained on the standard KIM zircons
369 were 0.11‰ for ¹⁸O/¹⁶O and 0.23‰ for ³⁰Si/²⁸Si (1 s.d.), which are commensurate with the
370 internal measurement errors, and better than reconnaissance O-isotope results obtained for the
371 Hyperion-II oxygen plasma source (59; SI Appendix, Fig. S7).

372

373 **Acknowledgements:**

374 This work was supported by NSF grants EAR-1447404 and EAR-1650033. The ion
375 microprobe facility at UCLA is partially supported by the Instrumentation and Facilities
376 Program, Division of Earth Sciences, NSF (EAR-1339051 and EAR-1734856). The LA-ICP-

377 MS instrument at the University of Rochester is partially supported by EAR-1545637. PB is
378 supported by the University of Chicago Chamberlin Postdoctoral Fellowship. We thank Jacob
379 Buettner for assistance and George Morgan for CL imaging. We thank Stephen Mojzsis and two
380 anonymous reviewers for careful and thoughtful comments and suggestions that improved the
381 clarity and content of the manuscript.

382
383 **References:**

- 384
385 1. Smith, JV (1981) The First 800 Million Years of Earth's History. *Phil. Trans. R. Soc.*
386 *Lond. A*, 301: 401-422.
387 2. Sleep NH, Zahnle KJ, Kasting JF, Morowitz HJ (1989) Annihilation of ecosystems by
388 large asteroid impacts on the early Earth. *Nature*, 342(6246): 139-142.
389 3. Maher KA, Stevenson DJ (1986) Impact frustration of the origin of life. *Nature*, 331:
390 612-614.
391 4. Froude DO, Ireland TR, Kinny PD, Williams IS, Compston W, Myers JS (1983) Ion
392 microprobe identification of 4,100-4,200 Myr-old terrestrial zircons. *Nature* 304: 616-
393 618.
394 5. Mojzsis SJ, Harrison TM, Pidgeon RT (2001) Oxygen-isotope evidence from ancient
395 zircons for liquid water at the Earth's surface 4,300 Myr ago. *Nature*, 409: 178-181.
396 6. Valley JW, Peck WH, King EM, Wilde SA (2002) A cool early Earth. *Geology*, 30: 351-
397 354.
398 7. Harrison TM (2009). The Hadean Crust: Evidence from >4 Ga Zircons. *Annual Review of*
399 *Earth and Planetary Sciences*, 37: 479-505.
400 8. Cavosie AJ, Valley JW, Wilde SA (2005) Magmatic $\delta^{18}\text{O}$ in 4400–3900 Ma detrital
401 zircons: a record of the alteration and recycling of crust in the Early Archean. *Earth*
402 *Planet Sci Lett*, 235: 663-681.
403 9. Sleep, N.H., Zahnle, K., Neuhoff, P.S., (2001) Initiation of clement surface conditions on
404 the earliest Earth. *Proc Natl Acad Sci*, 98: 3666-72.
405 10. Abramov O, Mojzsis SJ (2009) Microbial habitability of the Hadean Earth during the late
406 heavy bombardment. *Nature* 459: 419-422.
407 11. Boehnke P, Harrison TM (2016) Illusory Late Heavy Bombardments. *Proc Natl Acad Sci*
408 113:10802–10806.
409 12. Bell, EA, Boehnke, P, Harrison, TM (2015) Potentially biogenic carbon preserved in a
410 4.1 billion-year-old zircon. *Proc Natl Acad Sci*, 112: 14518–14521.
411 13. Opfergelt S, Delmelle P (2012) Silicon isotopes and continental weathering processes:
412 Assessing controls on Si transfer to the ocean. *Comptes Rendus Geoscience*, 344: 723-
413 738.
414 14. Opfergelt, S. et al. (2012) Silicon isotopes and the tracing of desilication in volcanic soil
415 weathering sequences, Guadeloupe. *Chemical Geology*, 326: 113-122.
416 15. Savage, PS, Armytage RMG, Georg RB, Halliday AN (2014) High temperature silicon
417 isotope geochemistry. *Lithos*, 190-191: 500-519.

- 418 16. Savage PS, Georg RB, Williams HM, Halliday AN (2013) The silicon isotope
419 composition of the upper continental crust. *Geochimica et Cosmochimica Acta* 109:384-
420 399.
- 421 17. Marin-Carbonne J, Robert F, Chaussidon M (2014) The silicon and oxygen isotope
422 compositions of Precambrian cherts: A record of oceanic paleo-temperatures?
423 *Precambrian Research* 247:223-234
- 424 18. Pollington AD, *et al.* (2016) Experimental calibration of silicon and oxygen isotope
425 fractionations between quartz and water at 250°C by in situ microanalysis of
426 experimental products and application to zoned low $\delta^{30}\text{Si}$ quartz overgrowths. *Chemical*
427 *Geology* 421:127-142.
- 428 19. Kleine BI, Stefánsson A, Halldórsson SA, Whitehouse MJ, & Jónasson K (2018) Silicon
429 and oxygen isotopes unravel quartz formation processes in the Icelandic crust.
430 *Geochemical Perspectives Letters*:5-11.
- 431 20. Abraham K, Hoffman A, Foley SF, Cardinal D, Harris C, Barth MG, André L (2011)
432 Coupled silicon–oxygen isotope fractionation traces Archaean silicification. *Earth and*
433 *Planet. Sci. Lett.*, 301(1-2): 222-230.
- 434 21. Savage PS *et al.* (2012) The silicon isotope composition of granites. *Geochimica et*
435 *Cosmochimica Acta*, 92: 184-202.
- 436 22. Poitrasson F, Zambardi T (2015) An Earth–Moon silicon isotope model to track silicic
437 magma origins. *Geochimica et Cosmochimica Acta* 167:301-312.
- 438 23. Savage PS, Georg RB, Williams, HM, Burton KW, Halliday AN (2011) Silicon isotope
439 fractionation during magmatic differentiation. *Geochimica et Cosmochimica Acta*, 75:
440 6124-6139.
- 441 24. Qin T, Wu F, Wu Z, Huang F (2016) First-principles calculations of equilibrium
442 fractionation of O and Si isotopes in quartz, albite, anorthite, and zircon. *Contributions to*
443 *Mineralogy and Petrology* 171(11) 10.1007/s00410-016-1303-3.
- 444 25. Bell EA, Harrison TM, McCulloch MT, Young ED (2011) Early Archean crustal
445 evolution of the Jack Hills Zircon source terrane inferred from Lu–Hf, 207Pb/206Pb, and
446 $\delta^{18}\text{O}$ systematics of Jack Hills zircons. *Geochimica et Cosmochimica Acta*, 75: 4816-
447 4829.
- 448 26. Valley JW, Kinny PD, Schulze DJ, Spicuzza MJ (1998) Zircon megacrysts from
449 kimberlite: oxygen isotope variability among mantle melts. *Contrib Mineral Petrol*
450 133:1-11.
- 451 27. Trail D, Bindeman IN, Watson EB, Schmitt AK (2009) Experimental calibration of
452 oxygen isotope fractionation between quartz and zircon. *Geochimica et Cosmochimica*
453 *Acta*, 73: 7110-7126.
- 454 28. O'Neil JR, Chappell BW (1977) Oxygen and hydrogen isotope relations in the Berridale
455 batholith. *J. geol. Soc. Lond.*, 33: 559-57
- 456 29. Chappell BW, White AJR (1992) I- and S-type granites in the Lachlan Fold Belt.
457 *Transactions of the Royal Society of Edinburgh: Earth Sciences* 83: 1-26.
- 458 30. André L, Cardinal, D, Alleman L, Moorbath S. (2006) Silicon isotopes in ~3.8 Ga West
459 Greenland rocks as clues to the Eoarchean supracrustal Si cycle. *Earth and Planetary*
460 *Science Letters*, 245: 162-173.
- 461 31. Robert F, Chaussidon M. (2006) A palaeotemperature curve for the Precambrian oceans
462 based on silicon isotopes in cherts. *Nature*, 443: 969-72.

- 463 32. Steinhoefel G, Horn I, von Blanckenburg F (2009) Micro-scale tracing of Fe and Si
464 isotope signatures in banded iron formation using femtosecond laser ablation.
465 *Geochimica et Cosmochimica Acta*, 73: 5343-5360.
- 466 33. Khan RMK, Sharma SD, Patil DJ, Naqvi S.M. (1996) Trace, rare-earth element, and
467 oxygen isotopic systematics for the genesis of banded iron-formations: Evidence from
468 Kushtagi schist belt, Archaean Dharwar Craton, India. *Geochimica et Cosmochimica*
469 *Acta*, 60: 3285-3294.
- 470 34. Zheng, YF (1991) Calculation of oxygen isotope fractionation in metal oxides. *Geochim.*
471 *Cosmochim. Acta*, 55: 2299-2307.
- 472 35. Wenner DB, Taylor Jr, HP (1973) Oxygen and hydrogen isotope studies of the
473 serpentinization of ultramafic rocks in oceanic environments and continental ophiolite
474 complexes. *American Journal of Science*, 273: 207-239.
- 475 36. Muehlenbachs K, Clayton, RN (1976) Oxygen Isotope composition of the oceanic crust
476 and its bearing on seawater. *J. of Geophys. Res.* 81, 4365-4369.
- 477 37. Holland, HD (1984) The Chemical Evolution of Atmospheres and Oceans. *Princeton*
478 *Univ. Press*, pp. 587.
- 479 38. Brengman LA (2015) Distinguishing primary versus secondary geochemical and silicon
480 isotope characteristics of Precambrian chert and iron formation. *Univ. Tennessee PhD*
481 *thesis 238 pp.*
- 482 39. Kemp AIS, et al. (2010) Hadean crustal evolution revisited: New constraints from Pb–Hf
483 isotope systematics of the Jack Hills zircons. *Earth and Planetary Science Letters*
484 296:45-56.
- 485 40. Benner SA, Kim H-J, Carrigan MA (2012) Asphalt, Water, and the Prebiotic Synthesis of
486 Ribose, Ribonucleosides, and RNA. *Accounts of Chemical research* 45:2025–2034.
- 487 41. Schopf JW, Kudryavtsev, AB, Agresti, DG, Wdowiak TJ, Czaja AD (2002) Laser-Raman
488 imagery of Earth's earliest fossils. *Nature* 416:73-76.
- 489 42. Manning CE, Mojzsis, SJ, Harrison, TM (2006) Geology, Age and Origin of Supracrustal
490 Rocks at Akilia, West Greenland. *American Journal of Science* 306:303-366.
- 491 43. Haggerty, SE, Raber E, Naeser CW (1983) Fission track dating of kimberlitic zircons.
492 *Earth and Planetary Science Letters*, 63: 41-50.
- 493 44. Ickert RB, Williams IS (2011) U–Pb zircon geochronology of Silurian–Devonian granites
494 in southeastern Australia: implications for the timing of the Benambran Orogeny and the
495 I–S dichotomy. *Australian Journal of Earth Sciences* 58: 501-516
- 496 45. Roddick JC, Compston W (1977) Strontium isotopic equilibration: a solution to a
497 paradox. *Earth and Planetary Science Letters* 34:238-246.
- 498 46. Williams IS (1992) Some observations on the use of zircon U-Pb geochronology in the
499 study of granitic rocks. *Second Hutton Symposium: The Origin of Granites and Related*
500 *Rocks* 83:447-458
- 501 47. Chen YD, Williams IS (1990) Zircon inheritance in mafic inclusions from Bega batholith
502 granites, southeastern Australia: An ion microprobe study. *Journal of Geophysical*
503 *Research* 95(B11):17787
- 504 48. Chappell BW, White AJR, Williams IS (1990) Excursion Guide B-1. Cooma Granodiorite
505 and Berridale Batholith. *Seventh International Conference on Geochronology,*
506 *Cosmochronology, and Isotope Geology*: 1-53.
- 507 49. Chappell BW, White AJR (1974) Two contrasting granite types. *Pacific Geology* 8, 173–
508 174.

- 509 50. Trail D, Tailby ND, Sochko M, Ackerson MR (2015) Possible Biosphere-Lithosphere
510 Interactions Preserved in Igneous Zircon and Implications for Hadean Earth.
511 *Astrobiology*, 15: 575-86.
- 512 51. Trail D, Tailby ND, Wang Y, Harrison, TM, Boehnke P (2017) Aluminum in zircon as
513 evidence for peraluminous and metaluminous melts from the Hadean to present.
514 *Geochemistry, Geophysics, Geosystems* 10.1002/2016GC006794 1-14.
- 515 52. Trail D., et al. (2015) Redox evolution of silicic magmas: Insights from XANES
516 measurements of Ce valence in Bishop Tuff zircons. *Chemical Geology*, 402: 77-88.
- 517 53. Trail D, et al. (2007) Constraints on Hadean zircon protoliths from oxygen isotopes, Ti-
518 thermometry, and rare earth elements. *Geochemistry, Geophysics, Geosystems* 8(6).
- 519 54. Georg RB, Reynolds BC, Frank M, Halliday AN (2006) New sample preparation
520 techniques for the determination of Si isotopic compositions using MC-ICPMS.
521 *Chemical Geology*, 235: 95-104.
- 522 55. Savage PS, Moynier F. (2013) Silicon isotopic variation in enstatite meteorites: Clues to
523 their origin and Earth-forming material. *Earth and Planetary Science Letters*, 361: 487-
524 496.
- 525 56. Young ED, Galy A, Nagahara H. (2002) Kinetic and equilibrium mass-dependent isotope
526 fractionation laws in nature and their geochemical and cosmochemical significance.
527 *Geochimica et Cosmochimica Acta*, 66: 1095–1104.
- 528 57. Bindeman IN, Bekker A, Zakharov O (2016) Oxygen isotope perspective on crustal
529 evolution on early Earth: A record of Precambrian shales with emphasis on
530 Paleoproterozoic glaciations and Great Oxygenation Event. *Earth and Planetary Science
531 Letters*, 437, 101-113
- 532 58. Valley JW, Kitchen N, Kohn MJ, Niendorf CR, Spicuzza MJ (1995) UWG-2, a garnet
533 standard for oxygen isotope ratios: Strategies for high precision and accuracy with laser
534 heating. *Geochimica et Cosmochimica Acta*, 59: 5223-5231
- 535 59. Liu M-C, McKeegan KD, Harrison TM, Jarzabinski G, Vltava L (2018) The Hyperion-II
536 radio-frequency oxygen ion source on the UCLA ims1290 ion microprobe: Beam
537 characterization and applications in geochemistry and cosmochemistry. *International
538 Journal of Mass Spectrometry*, 424: 1-9

539
540

541 **Figure legends**

542

543 **Figure 1.** Schematic cartoon of Si and O isotope co-variation during fluid alteration and
544 precipitation processes. Chemical weathering, hydration, seawater silica precipitation, may have
545 different trajectories in Si-O isotope space (BSE = Bulk Silicate Earth). Note that ‘non-
546 equilibrium silicification’ has no specific vector or slope as this process can be highly variable
547 due to the different behavior of these elements under different rock/water ratios and at different
548 temperatures (19). Banded Iron Formations may be enriched in ^{18}O and depleted in ^{30}Si (not
549 shown).

550

551 **Figure 2.** Our MC-ICP-MS results showing that mantle-derived zircon megacrysts Mud Tank
552 carbonatite (Australia), Kimberley pool (South Africa), and Orapa Kimberlite (Botswana) yield
553 an average $\delta^{30}\text{Si}$ value of -0.38 ± 0.02 ‰ (1 s.d.). The top of the figure shows the Si isotopic

554 difference between zircon, quartz, and WR for the LFB I-type Jindabyne tonalite analyzed here;
555 $\Delta^{30}\text{Si}(\text{WR-zircon})$ is 0.37 ‰.

556
557 **Figure 3.** Histograms showing $\delta^{30}\text{Si}$ differences of zircons from 10 LFB granitoids and the
558 Duluth Gabbro (SI Appendix, Table S3). The bin sizes are 0.2 ‰, commensurate with the 1 s.e.
559 of our ion microprobe measurements. Some S-types contain measured $\delta^{30}\text{Si}$ values down to -1.5
560 ‰, while W060, for example, is largely indistinguishable from the $\delta^{30}\text{Si}$ of our I-type samples.
561 The A-type and zircons show broadly restricted ranges in $\delta^{30}\text{Si}$, when compared to S- and I-type
562 zircons. Whole Rock $\delta^{30}\text{Si}$ for S-, I-, and A-type LFB granitoids (21) can be found in Fig S1.
563 The mantle zircon field is -0.38 ± 0.02 ‰, after Figure 2. Histograms for zircon $\delta^{18}\text{O}$ values from
564 individual hand samples can be found in SI Appendix, Fig. S3.

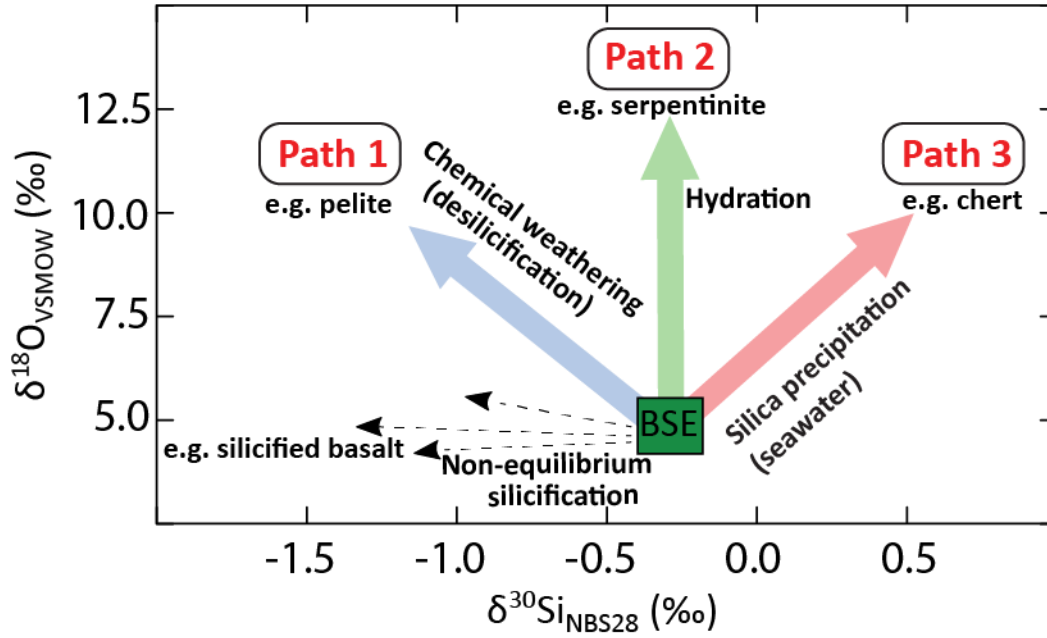
565
566 **Figure 4.** Zircon LFB $\delta^{18}\text{O}$ vs. $\delta^{30}\text{Si}$, with annotated path trajectories after Figure 1. The
567 ‘mantle’ zircon fields are $+5.3\pm 0.3$ ‰ and -0.38 ± 0.02 ‰ for $\delta^{18}\text{O}$ (26) and $\delta^{30}\text{Si}$ (Fig. 2),
568 respectively. Average $\delta^{18}\text{O}$ values for S-type zircons are +8.8 ‰, consistent with a whole rock
569 value of $\delta^{18}\text{O} > 10$ ‰ (28). The zircon $\delta^{18}\text{O}$ values from I-type rocks yield average values +7.5
570 ‰, consistent with WR values of < 10 ‰ (SI Appendix, Table S3). Path 2 may also indicate a
571 balance between assimilation/derivation between chert-like, “path 3” and pelite-like “path 1”
572 protoliths, both of which have high $\delta^{18}\text{O}$.

573
574 **Figure 5 (a)** Plot of $\delta^{30}\text{Si}$ vs. $\delta^{18}\text{O}$ for single Hadean (≥ 4.0 Ga) and Archean zircon, with
575 schematic weathering paths from Figure 1, revealing isotopic heterogeneities in both age suites.
576 Mantle-derived zircon yield values of $+5.3\pm 0.3$ (26) and -0.38 ± 0.02 ‰ (Fig. 1) for $\delta^{18}\text{O}$ and
577 $\delta^{30}\text{Si}$, respectively. **(b)** Zircon $\delta^{30}\text{Si}$ plotted against age showing fractionations away from mantle
578 values. Error bars are 1 s.e. (SI Appendix, Table S4) or the standard deviation of multiple ion
579 microprobe analyses on a single grain, whichever is larger. The ‘mantle’ zircon field is drawn –
580 and reliant upon – high precision MC-ICP-MS data zircon results (SI Appendix, Table S2).

581
582
583
584
585
586
587
588
589
590
591
592
593
594
595
596
597
598
599

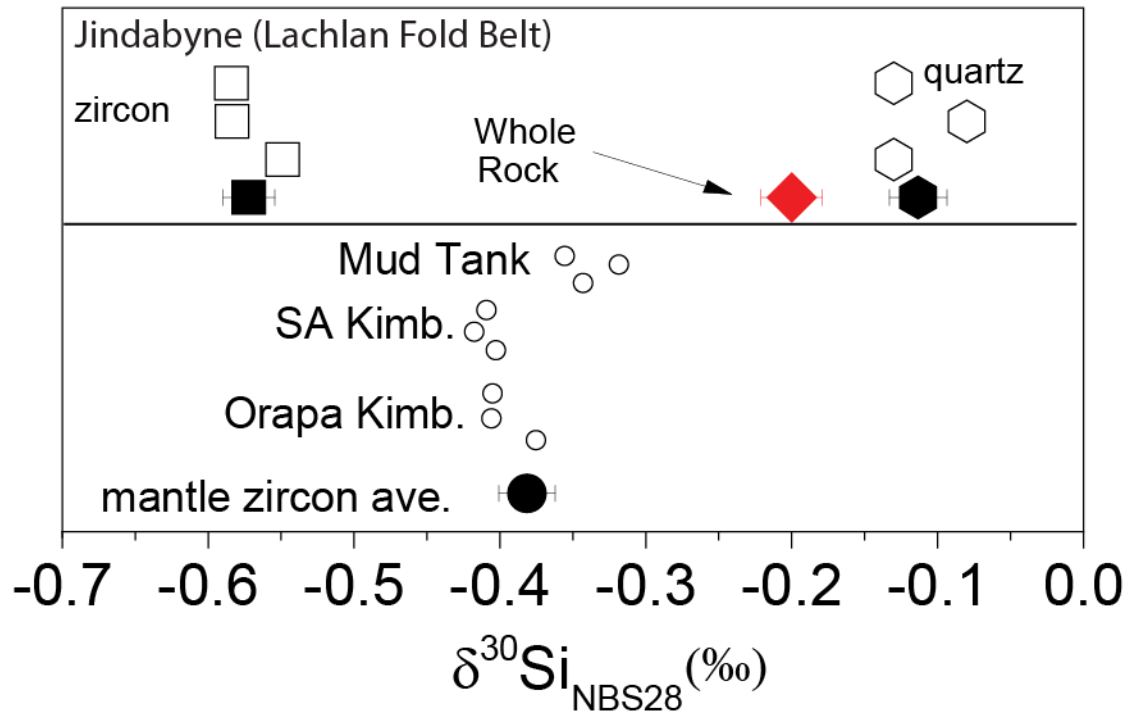
600
601
602
603
604

Figure 1



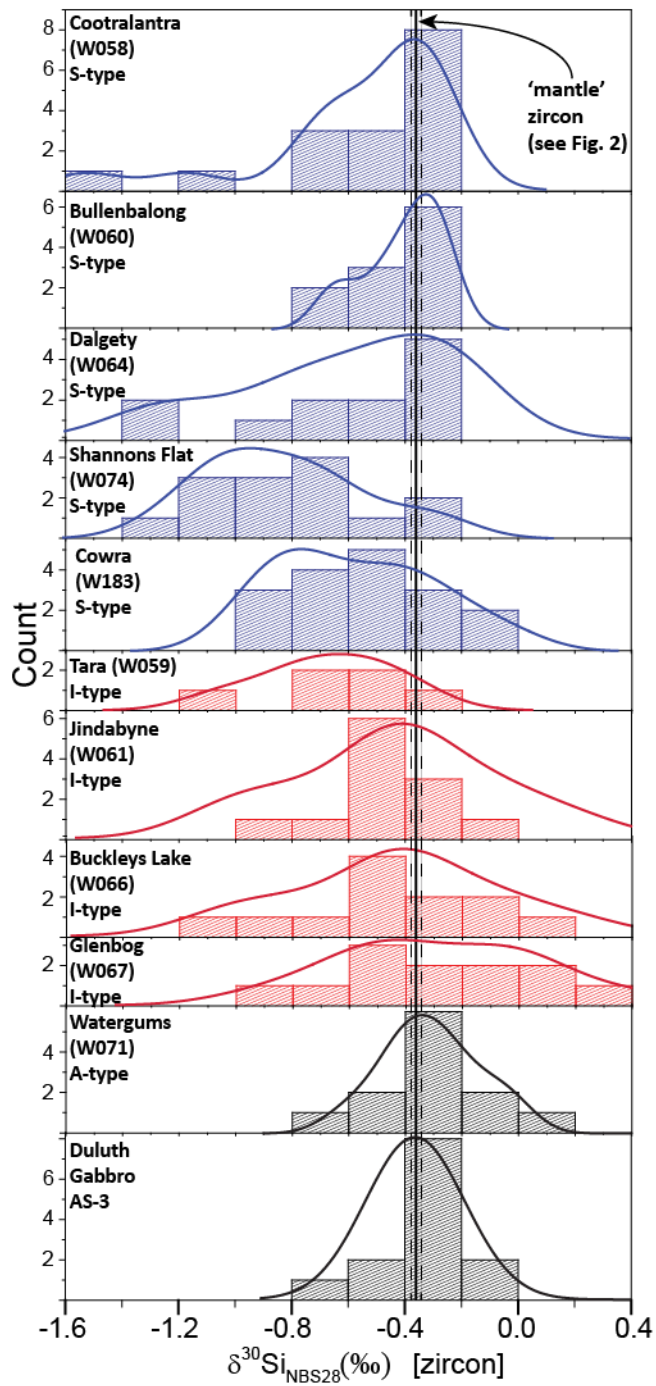
605
606
607
608
609
610
611
612
613
614
615
616
617
618
619
620
621
622
623
624
625
626
627
628
629

630 Figure 2



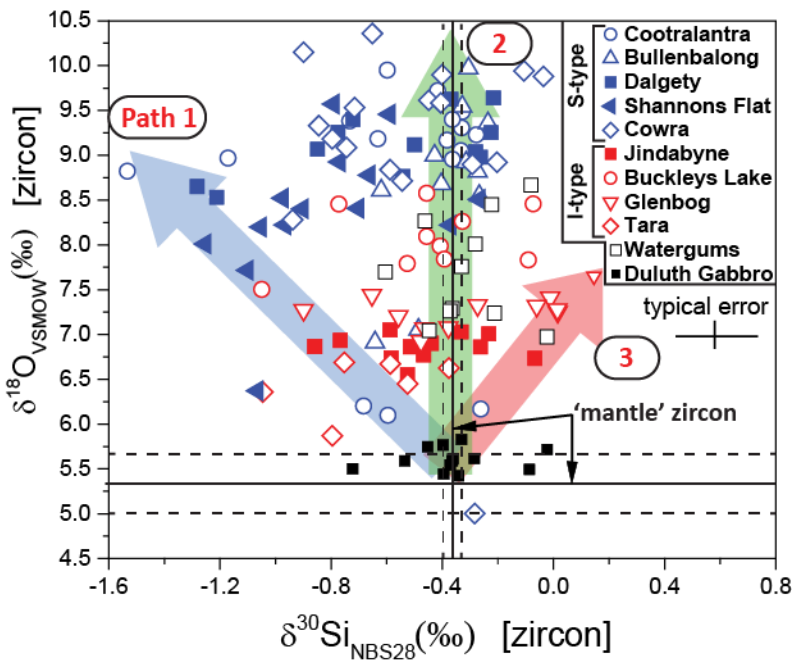
631
632
633
634
635
636
637
638
639
640
641
642
643
644
645
646
647
648
649
650
651
652
653
654
655
656

657 Figure 3
658
659
660
661



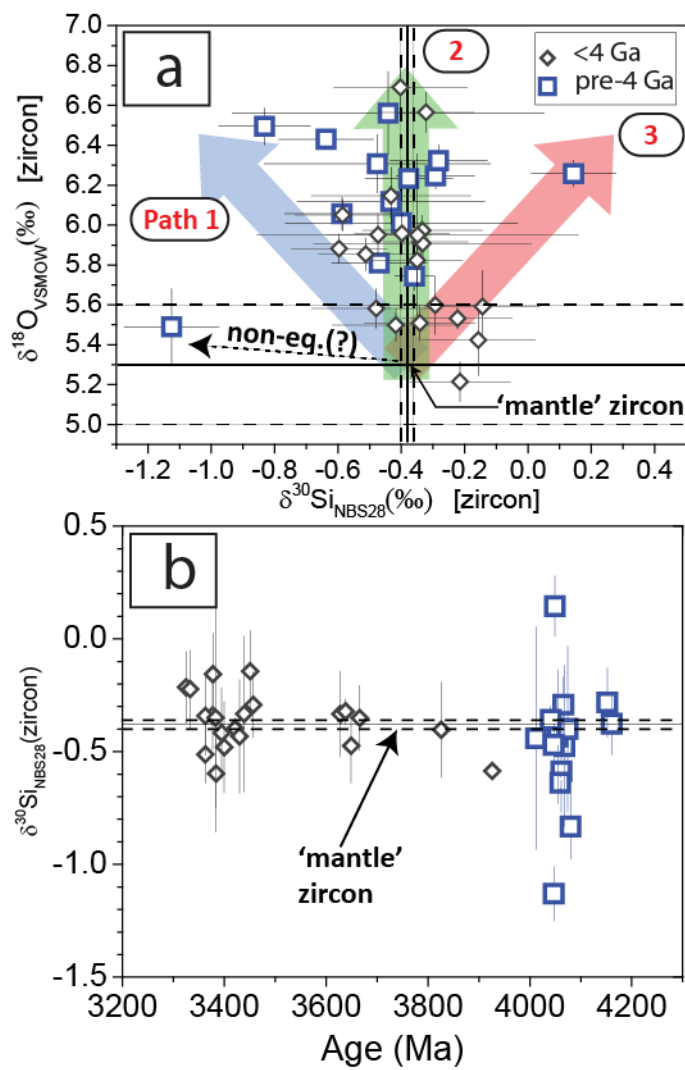
662
663
664
665
666

667 Figure 4
668
669
670
671
672
673
674
675
676
677
678
679



680
681
682
683
684
685
686
687
688
689
690
691
692
693
694
695
696

697 Figure 5
698
699



700